Effect of Droplet Morphology on Growth Dynamics and Heat Transfer during Condensation on Superhydrophobic Nanostructured Surfaces

Nenad Miljkovic,[†] Ryan Enright,[†,‡] and Evelyn N. Wang[†,*]

[†]Department of Mechanical Engineering, Massachusetts Institute of Technology, 77 Massachusetts Avenue, Cambridge, Massachusetts 02139, United States, and
[‡]Stokes Institute, University of Limerick, Limerick, Ireland

ABSTRACT Condensation on superhydrophobic nanostructured surfaces offers new opportunities for enhanced energy conversion, efficient water harvesting, and high performance thermal management. These surfaces are designed to be Cassie stable and favor the formation of suspended droplets on top of the nanostructures as compared to partially wetting droplets which locally wet the base of the nanostructures. These suspended droplets promise minimal contact line pinning and promote passive droplet shedding at sizes smaller than the characteristic capillary length. However, the gas films underneath such droplets may significantly hinder the overall heat and mass transfer performance. We investigated droplet growth dynamics on superhydrophobic nanostructured surfaces to elucidate the importance of droplet morphology on heat and mass transfer. By taking advantage of well-controlled functionalized silicon nanopillars, we observed the growth and shedding behavior of suspended and partially wetting droplets on the same surface during condensation. Environmental scanning electron microscopy was used to demonstrate that initial droplet growth rates of partially wetting droplets were 6× larger than that of suspended droplets. We subsequently developed a droplet growth model to explain the experimental results and showed that partially wetting droplets had 4−6× higher heat transfer rates than that of suspended droplets. On the basis of these findings, the overall performance enhancement created by surface nanostructuring was examined in comparison to a flat hydrophobic surface. We showed these nanostructured surfaces had 56% heat flux enhancement for partially wetting droplet morphologies and 71% heat flux degradation for suspended morphologies in comparison to flat hydrophobic surfaces. This study provides insights into the previously unidentified role of droplet wetting morphology on growth rate, as well as the need to design Cassie stable nanostructured surfaces with tailored droplet morphologies to achieve enhanced heat and mass transfer during dropwise condensation.

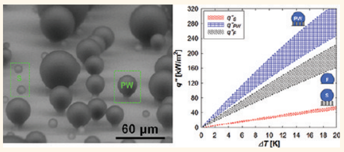

KEYWORDS: dropwise condensation · ESEM · droplet growth dynamics · wetting · superhydrophobic · nanostructure design · heat transfer enhancement

Vapor condensation is a phenomenon widely observed in nature and an essential part of energy conversion,[1] water harvesting,[2,3] and thermal management systems.[4−7] Improvements in heat and mass transfer during this phase change process, therefore, can lead to a considerable conservation of natural and economic resources. When water vapor condenses on a surface, the condensate can form either a liquid film or distinct droplets, depending on the surface wettability. The latter, termed dropwise condensation, is desired since the droplets can be efficiently removed from the surface, which significantly increases heat and mass transfer performance.[8] Recent research has focused on using a combination of chemical functionalization and roughness to create superhydrophobic surfaces for dropwise condensation, whereby droplets easily roll off the surface due to gravity upon reaching a critical size (~2 mm).[9−11]

A recent study, however, showed that when small droplets (~10−100 μm) merge on superhydrophobic nanostructured surfaces, droplets can spontaneously eject *via* the release of excess surface energy independent of gravity.[12,13] This phenomenon is attributed to the nanoscale surface roughness (~100 nm), which enhances the hydrophobicity, and thereby decreases droplet pinning to the surface.[14] Droplet removal by this mechanism is highly desirable due to the increased number of small droplets[15] which efficiently transfer the majority of the heat from the surface.[1,16,17] A number of works have since fabricated superhydrophobic nanostructured surfaces to achieve spontaneous droplet removal.[7,18−22] These surfaces were designed to be Cassie stable such that droplets are *suspended* (S) on gas-filled nanostructures[23] to have minimal contact line pinning due to the nanoscale roughness, which is in contrast to Wenzel stable surfaces with droplets that wet the cavities of the nanostructures[24] and cannot be removed *via* droplet ejection due to the highly pinned contact line. Recently, two distinct wetting morphologies on Cassie stable surfaces during condensation have

* Address correspondence to enwang@mit.edu.

Received for review December 7, 2011 and accepted January 31, 2012.

10.1021/nn205052a

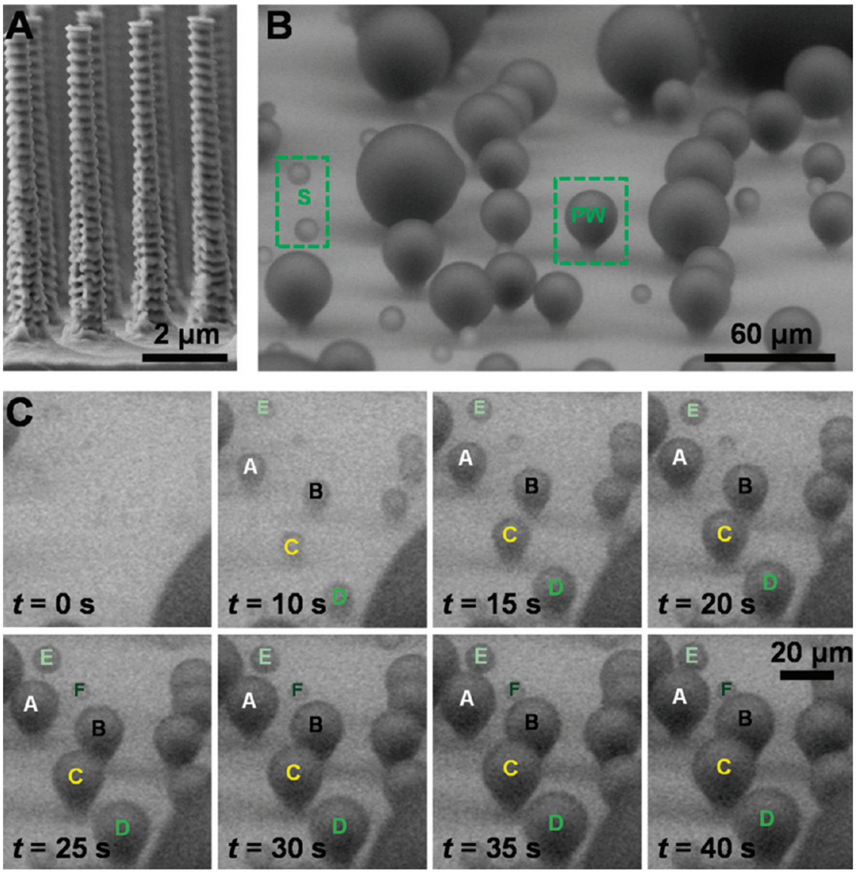

Figure 1. (A) Scanning electron micrograph (SEM) of an array of equidistant superhydrophobic silicon nanopillars with diameters, heights, and spacings of d = 300 nm, h = 6.1 μm, and l = 2 μm, respectively. Nanoscale scallop features exist on the pillar sidewalls due to the DRIE fabrication process. (B) Environmental scanning electron micrograph (ESEM) of water condensation on (A) showing both *partially wetting* (PW) and *suspended* (S) droplets (P = 1200 ± 12 Pa, T_s = 282 ± 1.5 K). See Supporting Information, videoS1. (C) Time lapse images of condensation captured *via* ESEM showing the difference in growth behavior between PW and S droplets. Droplets A, B, C, and D are in the PW state, whereas E and F are in the S state. See Supporting Information, videoS2.

been reported where, in addition to S droplets, *partial wetting* (PW) droplets that locally wet the substrate between the pillars (*i.e.*, with liquid-filled nanostructures under a portion of the nominally Cassie droplet)[25−27] can exist. While to date it has been unclear whether PW droplets can undergo droplet ejection, S droplets were considered to be desired due to their decreased contact line pinning to the nanostructured surface.[3,15,18,20] However, the gas layer beneath these droplets can act as a barrier to heat transfer and can degrade overall heat and mass transfer performance, which was not considered in previous studies.

Here, we investigated *in situ* water condensation on superhydrophobic nanostructured surfaces using environmental scanning electron microscopy (ESEM).[5,7,15,19−21,25,26,28−30] The surfaces were designed to be Cassie stable and allowed droplets of both S and PW morphologies to coexist due to the presence of nanoscale scallop features (∼100 nm). These surfaces allowed characterizations and direct comparisons of growth rates and removal mechanisms for both droplet morphologies under identical condensation conditions. The experimental results showed that while both S and PW droplets ejected at identical length scales, the growth rate of PW droplets was 6× larger compared to that of S droplets. This effect was further highlighted with experiments demonstrating S to PW droplet transitions, which showed a 2.8× increase in growth rate due to the change in wetting morphology. Accordingly, the heat transfer of the PW droplet was 4−6× higher than that of the S droplet. On the basis of these results, we compared the overall surface heat and mass transfer performance enhancement created by surface structuring with that of a flat hydrophobic surface. We showed that these nanostructured surfaces had 56% heat flux enhancement for PW droplet morphologies and 71% heat flux degradation for S morphologies in comparison to flat hydrophobic surfaces. In contrast to previous studies, we show that designing Cassie stable superhydrophobic nanostructured surfaces is not the only requirement for efficient dropwise condensation and that the droplet morphology prior to shedding must be carefully considered to achieve enhanced heat and mass transfer.

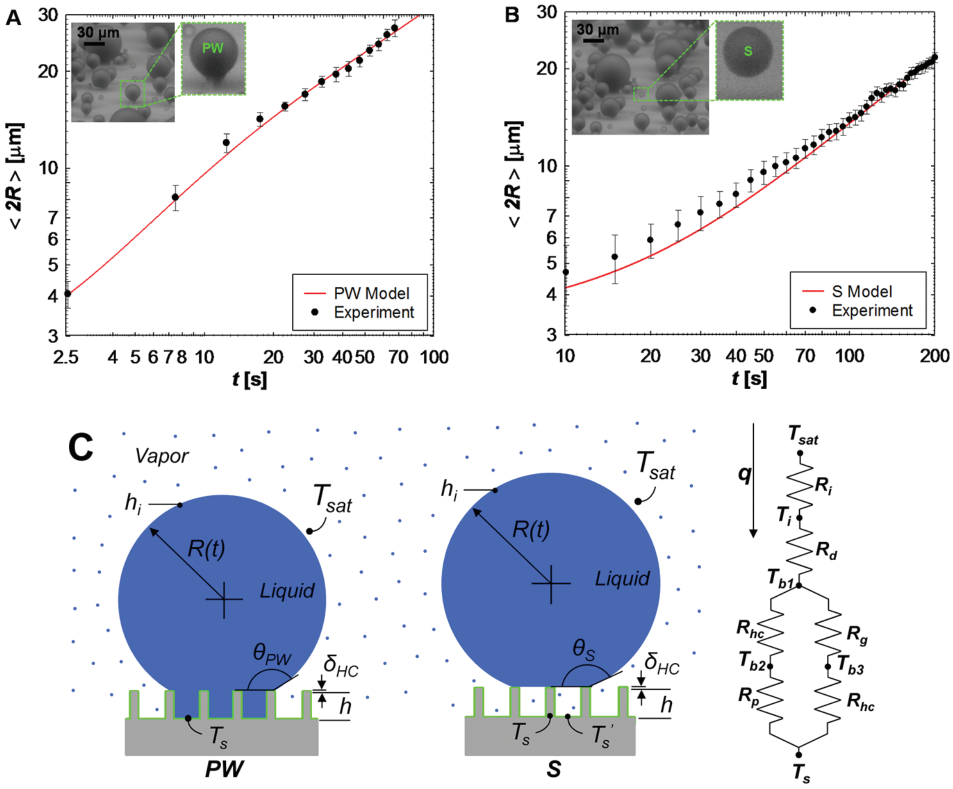

Figure 2. Time evolution of the average droplet diameter (⟨2*R*⟩). (A) For the PW droplet, at early stages (⟨2*R*⟩ < 12 μm), the rapid growth is due to good thermal contact between the droplet base and the substrate (T_s). Inset: ESEM image of a PW droplet. (B) S droplet has a slower growth rate than the PW droplet due to poor thermal contact between the base and substrate. At later stages (⟨2*R*⟩ ≥ 12 μm), the S and PW growth rates converge due to the dominant conduction thermal resistance of the droplet (R_d). Inset: ESEM image of a S droplet. Experimental data (black circles) were obtained from ESEM video ($P = 1200 \pm 12$ Pa, $T_s = 282 \pm 1.5$ K) (see Supporting Information, videoS1 and S2). The theoretical prediction (red line) was obtained from the droplet growth model (for model derivation and parameters, see section S6 of Supporting Information). (C) PW and S droplet model schematics and thermal resistance diagram showing the liquid–vapor interface (R_i), droplet conduction (R_d), hydrophobic coating (R_{hc}), pillar (R_p), and gap (R_g) thermal resistances.

RESULTS AND DISCUSSION

To study the effects of droplet wetting morphology on growth rate and overall heat transfer, we fabricated silicon nanopillar surfaces (Figure 1A) with diameters of d = 300 nm, heights of $h = 6.1$ μm, center-to-center spacings of $l = 2$ μm (solid fraction $\varphi = \pi d^2/4l^2 = 0.018$ and roughness factor $r = 1 + \pi dh'/l^2 = 3.26$) using e-beam lithography and deep reactive ion etching (DRIE). The DRIE fabrication process was used to create nanoscale roughness (scallops) on the sides of the pillars. The surfaces were subsequently functionalized using chemical vapor deposition of (tridecafluoro-1,1,2,2-tetrahydrooctyl)-1-trichlorosilane to create Cassie stable superhydrophobic surfaces (see Methods section for details).

Droplet growth on the surfaces was characterized using ESEM at a water vapor pressure $P = 1200 \pm 12$ Pa and substrate temperature $T_s = 9 \pm 1.5$ °C (see Methods section for details). Figure 1B shows the two distinct droplet morphologies, PW and S, on the structured surface. PW droplets nucleated within a unit cell (area between 4 pillars), and while growing beyond the confines of the unit cell, their apparent contact angle increased and they spread across the tops of the pillars in the shape of a balloon with a liquid bridge at the base of the pillars. Before coalescence with neighboring droplets, an increasing proportion of the droplet contact area was in the composite state and demonstrated an apparent contact angle of $\theta_{PW} = 164 \pm 4°$ for $\langle R \rangle > 15$ μm. S droplets nucleated and grew on the tops of the pillars in a spherical shape with a constant apparent contact angle of $\theta_S = 164 \pm 6°$. At these droplet sizes ($\langle R \rangle \sim l$), the S wetting configuration is typically energetically unfavorable due to a Laplace pressure instability mechanism[31] but is attributed here to the presence of the nanoscale scallop features on the pillar sides that pin the contact line (see Supporting Information, sections S3 and S4). Figure 1C shows time lapse images of both PW and S droplets, which highlights the drastic difference in droplet morphology and growth rates on the surface (see Supporting Information, videoS2). As the droplets grew and began to interact with each other, removal *via* coalescence-induced droplet ejection[12,13,15] was observed for both S and PW droplets. The results suggest that the contact line pinning force for both morphologies is in fact below the critical threshold for ejection (see Supporting Information, section S5 and videoS1).

The experimentally obtained average droplet diameters as a function of time for the PW and S morphologies are shown in Figure 2A,B, respectively. The growth rate of the S droplet was initially 6× lower than that of the PW droplet for $\langle R \rangle < 6\ \mu$m. As the droplets reached radii $\langle R \rangle > 6\ \mu$m, the growth rates for both morphologies became comparable, which suggests a similar mechanism limiting droplet growth at the later stages.

To provide insight into the experimental results and capture the growth dynamics related to the different droplet morphologies, we developed a thermal resistance-based droplet growth model. The model, which accounts for the presence of hydrophobic pillar structures, is an important extension of a previous model suitable for dropwise condensation on flat hydrophobic surfaces.[10] Figure 2C shows schematics of the PW and S droplets with the associated parameters used in the growth model. Heat is first transferred from the saturated vapor to the liquid–vapor interface through resistances associated with the droplet curvature (R_c) and liquid–vapor interface (R_i). Heat is then conducted through the droplet and the pillars to the substrate through resistances associated with the droplet (R_d), hydrophobic coating (R_{hc}), pillars (R_p), and gap (R_g). Marangoni and buoyancy effects are neglected since the droplets are sufficiently small so that conduction is the dominant mode of heat transfer.[32,33] Accounting for all of the thermal resistances, the heat transfer rate, q, through a single condensing droplet is (see Supporting Information, section S6)

$$q = \frac{\Delta T}{R_{\text{tot}}} = \pi R^2 \left(\Delta T - \frac{2T_{\text{sat}}\sigma}{Rh_{\text{fg}}\rho_{\text{w}}} \right) \Big/ \frac{1}{2h_{\text{i}}(1 - \cos\theta)} + \frac{R\theta}{4k_{\text{w}}\sin\theta} + \frac{1}{k_{\text{HC}}\sin^2\theta}\left[\frac{k_{\text{P}}\phi}{\delta_{\text{HC}}k_{\text{P}} + hk_{\text{HC}}} + \frac{k_{\text{w}}(1-\phi)}{\delta_{\text{HC}}k_{\text{w}} + hk_{\text{HC}}}\right]^{-1} \quad (1)$$

where R_{tot} is the total thermal resistance through the droplet, R is the droplet radius, ρ_{w} is the liquid water density, h_{fg} is the latent heat of vaporization, T_{sat} is the vapor saturation temperature, σ is the water surface tension, ΔT is the temperature difference between the saturated vapor and substrate ($T_{\text{sat}} - T_{\text{s}}$), δ_{HC} and h are the hydrophobic coating thickness (~1 nm) and pillar height, respectively, k_{HC}, k_{w}, and k_{P} are the hydrophobic coating, water, and pillar thermal conductivities, respectively, and h_{i} is the interfacial condensation heat transfer coefficient.[34] The first, second, and third terms in the denominator represent the liquid–vapor interface (R_i), droplet conduction (R_d), and pillar-coating-gap (P-C-G) thermal resistances (R_p, R_{hc}, R_g), respectively (Figure 2C). The heat transfer rate is related to the droplet growth rate dR/dt by

$$q = \dot{m}h_{\text{fg}} = \rho_{\text{w}}h_{\text{fg}}\frac{dV}{dt} = \frac{\pi}{3}\rho_{\text{w}}h_{\text{fg}}\frac{d}{dt}\{(1 - \cos\theta)^2(2 + \cos\theta)R^3\} \quad \textbf{(2)}$$

During early stages of growth ($R < 6\ \mu$m), the conduction resistance (R_d) is negligible compared to the other thermal resistances. Therefore, for the PW droplet, the pillar ($R_p + R_{hc}$) and liquid bridge ($R_g + R_{hc}$) resistances dominate the heat and mass transfer process. However, for the S droplet, the only conduction path is through the pillars ($R_p + R_{hc}$), which results in a higher total thermal resistance and the observed 6× lower initial growth rate. Note that the pillar (R_p), coating (R_{hc}), and gap (R_g) thermal resistances are not the only reasons for the divergent growth behavior of the two droplet morphologies. The higher initial contact angle of S morphology (see Supporting Information, section S3) contributes to its slower growth rate due to a lower droplet basal contact area. As both droplet morphologies reach a critical radius, $R_{cd} \approx 6\ \mu$m, the conduction resistance (R_d) begins to dominate and limit the growth rate in both cases.[32] A theoretical estimate of R_{cd} was obtained by balancing the conduction resistance through the droplet, $R_d = R\theta/(4\pi R2k_w \sin\theta)$, with the interfacial, $R_i = 1/(2\pi R^2 h_i(1 - \cos\theta)$, and P-C-G, $R_{\text{P-C-G}} \sim k_{\text{P}\varphi}/(k_{\text{HC}}\pi R^2 \sin 2\theta(\delta_{\text{HC}}k_{\text{P}} + hk_{\text{HC}}))$ thermal resistances.[35] The interfacial and conduction resistances become equivalent at a radius $R_{cd} = 4k_w \sin\theta(R_i + R_{\text{P-C-G}})/\theta \approx 6\ \mu$m, which is in good agreement with our experiments.

The results from the model (red lines) are also shown in Figure 2A,B and are in excellent agreement with the experiments (black circles). Model solutions were obtained for $\Delta T = 0.12$ K, where ΔT was chosen based on the best fit between the model and experimental growth rate data. The approximate value of ΔT from the experiments was $\Delta T = T_{\text{sat}}(P = 1200\ \text{Pa}) - 282.15 \pm 1.5\ \text{K} = 0.65 \pm 1.5$ K. Therefore, the value used in the model is within the error of the experimental apparatus. In addition, the small value of ΔT is consistent with the assumption that only molecules near the substrate contribute to the phase change process; that is, the local vapor pressure is lower than the measured bulk vapor pressure.[28]

In order to gain further insight, we compared the experimental results with the power law exponent model.[13,36−42] When droplet dimensions are larger than the surface pattern length scales ($\langle R \rangle > 2\ \mu$m), droplets grow as breath figures on a surface with an expected average droplet radius of $\langle R \rangle = \rho t^{\alpha}$, where α, the power law exponent, ranges from 0 to 1 depending on the droplet, substrate dimensions, and growth limiting conditions. During initial growth without coalescence, the power law exponent was $\alpha_{\text{PW}} = 0.78 \pm 0.02$ and $\alpha_{\text{S}} = 0.46 \pm 0.03$ for the PW and S drops, respectively. Both values were within the range of 0 to 1 but differ from the expected 1/3 power law.[40] This result indicates that vapor diffusion to the droplet interface was not the limiting growth mechanism; instead, a kinetic barrier was formed due to the low ESEM pressures (P = 1200 Pa).[28] When the average droplet diameter $\langle 2R \rangle$ reached the coalescence length,

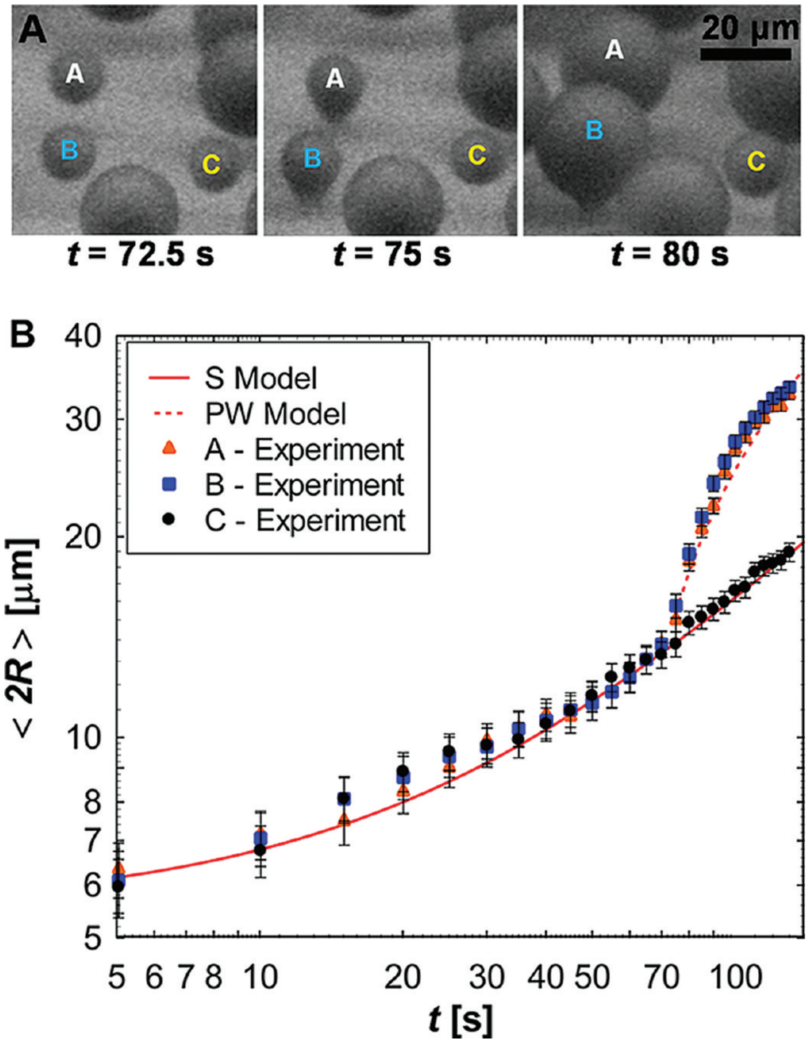

Figure 3. (A) Time lapse images of S to PW droplet transitions captured *via* ESEM showing the difference in growth behavior. Droplets A and B transition from the S to PW state, while droplet C remains in the S state throughout (see Supporting Information, videoS3). (B) Time evolution of the average droplet diameter ($\langle 2R \rangle$) for droplets A, B, and C. Initially ($t < 75$ s), all three droplets grow in the S state. Upon transition ($t = 75$ s), the growth rates of droplets A and B rapidly increased due to better thermal contact between the base of the droplet and the substrate. Additionally, subcooling due to a constriction resistance between the pillars ($T_s - T_s' = 0.044$ K) contributes to the growth behavior after transition. Experimental data (symbols) were obtained using ESEM ($P = 1200$ Pa, $T_s = 282 \pm 1.5$ K). Theoretical results were obtained using the droplet growth model of S droplets (solid red line) and PW droplets (dotted red line). For model derivation, see section S6 of Supporting Information.

both morphologies grew at a power law exponent of $\alpha_{PW} = \alpha_S = 0.05 \pm 0.15$ as expected; that is, the average diameter was constant due to coalescence-induced droplet ejection.[13]

Transitioning Droplets. In certain cases when the nanoscale scallop features on the pillars could not pin the droplet contact line, we observed S droplets transitioning to PW droplets (Figure 3A) (see Supporting Information, videoS3). This phenomenon further demonstrated the importance of the droplet wetting morphology on growth rate. Figure 3B shows the growth rate of three distinct S droplets, two of which underwent transition into the PW state. Upon transition, a liquid bridge formed between the droplet and substrate and the apparent contact angle decreased. The growth rate of these droplets increased by 2.8× compared to the S droplet immediately after transition. The transitioned growth rate ($dR/dt = 0.34$ μm/s) exceeded the steady growth rate of a comparably sized PW droplet ($dR/dt = 0.18$ μm/s), indicating that the driving potential for growth was larger. The increased rate was attributed to a larger substrate–vapor temperature difference ($T_{sat} - T_s$) due to additional subcooling from the constriction resistance at the base of the pillars ($T_s - T_s'$).[35] By determining the average temperature at the base between pillars using a spatial conduction resistance and incorporating the additional surface subcooling into the droplet growth model, the theoretical results show excellent agreement with the experiments (Figure 3B) (see section S7 of Supporting Information). Note that, at these transitioning length scales ($\sim 10^{-6}$ m), surface diffusion growth due to adsorbed atoms on the substrate is negligible and cannot account for the rapid increase in growth.[43–45]

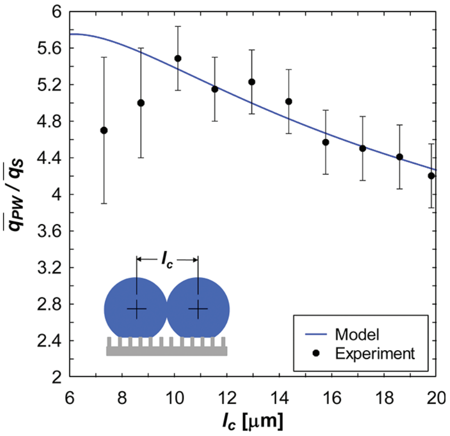

Figure 4. Individual droplet heat transfer ratio of PW to S droplets as a function of coalescence length, l_c. The PW droplets were 4–6× as effective as S droplets at heat removal during the dropwise condensation process due to better thermal contact between the droplet base and substrate. The large contact angle of both droplet morphologies results in small pinning forces at the contact line, allowing for coalescence-induced droplet shedding at coalescence lengths of 10 ± 2 μm. Heat transfer ratio data (black circles) was obtained from droplet growth experiments (Figure 2). Theoretical results (blue line) were obtained using the droplet growth model (see section S6 of Supporting Information). Inset: Schematic defining coalescence length.

Implications to Heat Transfer. On the basis of the understanding developed for individual droplet growth rates, we investigated the heat and mass transfer performance of the two distinct droplet morphologies. To quantify the difference in performance prior to coalescence-induced ejection, the total heat removed Q by the individual droplet was determined

$$Q = \int_{R^*}^{l_c/2} q\,dt = \frac{1}{3}\pi\rho_w h_{fg}(1-\cos\theta)^2(2+\cos\theta)\left(\frac{l_c}{2}\right)^3 \qquad (3)$$

where l_c is the coalescence length or, alternatively, can be considered the coalescing droplet diameter when droplets merge and shed from the surface.[13] R^* is the critical droplet radius for nucleation, which is approximated as zero due to its small magnitude (~10 nm). The ratio of the heat transfer rates for individual PW and S droplets, q_{PW}/q_S, is therefore approximated by

$$\frac{\overline{q_{PW}}}{\overline{q_S}} = \frac{\dfrac{Q_{PW}}{\tau_{PW}}}{\dfrac{Q_S}{\tau_S}} = \frac{(1-\cos\theta_{PW})^2(2+\cos\theta_{PW})\tau_S}{(1-\cos\theta_S)^2(2+\cos\theta_S)\tau_{PW}} \qquad (4)$$

where θ_{PW} and θ_S are the PW and S contact angles at coalescence, respectively, and τ_{PW} and τ_S are the PW and S droplet coalescence times (times at which coalescence occurs) corresponding to a coalescence length l_c, respectively. The coalescence times for the experimental and modeling results in Figure 4 were obtained from the growth rates in Figures 2 and 3. The higher error at lower coalescence lengths is due to the larger deviation between experimental and model growth rates for the S morphology, as well as larger experimental error associated with ESEM measurements for small droplet sizes.

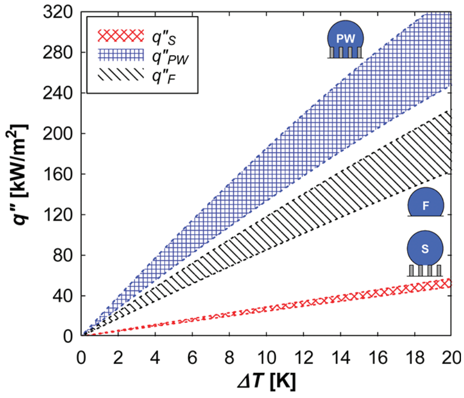

Figure 5. Theoretical steady state overall surface heat flux (q'') *versus* temperature difference (ΔT) for surfaces having distinct PW, S (h = 6.1 μm, l = 2 μm, d = 300 nm, φ = 0.0177), and F droplet morphologies. Model results were obtained by using droplet distribution theory with the developed droplet growth model (eq 13). Dotted lines represent error bounds associated with uncertainty in the coalescence length, l_c. Model parameters: P = 4 kPa, $l_{c,PW} = l_{c,S} = 10 \pm 2$ μm, $l_{c,F} = 28 \pm 7$ μm. When compared to the flat surface, there is an average 56% heat flux *enhancement* for the PW morphology and an average 71% heat flux *degradation* for the S morphology.

Figure 4 shows the heat transfer ratio model overlaid with experiments, where a 4–6× droplet heat transfer increase during dropwise condensation was demonstrated for PW compared to S droplets. As expected, the increased thermal resistance associated with the S droplet morphology decreases the growth rate and, as a result, severely limits individual S droplet heat transfer when compared to its PW counterpart. The heat transfer enhancement diminishes at larger coalescence lengths due to the increasing droplet conduction thermal resistance for both droplet morphologies, resulting in similar growth rates. Figure 4 indicates that meeting the criteria for Cassie stable surfaces is not the only requirement for heat and mass transfer enhancement. In fact, preferential formation of Cassie droplets with the S morphology can even degrade total surface heat and mass transfer performance when compared to a flat (non-nanostructured) hydrophobic surface, which is investigated in the next section.

Comparison to a Flat Hydrophobic Surface. The insights gained regarding individual droplet wetting morphology led to an investigation of the overall performance enhancement created by nanostructuring compared to a flat (no surface structuring) hydrophobic surface. Specifically, we aimed to address whether the benefit of droplet departure below the characteristic capillary length created by nanostructuring outweighs the disadvantage of reduced growth rates due to the increased thermal resistance associated with the S droplet morphology.

Additional ESEM droplet growth studies were performed on a flat hydrophobic surface for comparison (see section S8 of Supporting Information). The flat surface sample consisted of a silicon substrate, functionalized by CVD as described above. Droplet growth on the flat surface was characterized using identical condensation conditions as the nanostructured surfaces and also showed good agreement with the thermal resistance model.

To compare the theoretical surface heat and mass transfer performance on the flat and nanostructured surfaces, we combined droplet size distribution theory, to account for the fraction of droplets on the surface of a given radius R, with the developed droplet growth model. For small droplets, the size distribution $n(R)$ is determined by[10]

$$n(R) = \frac{1}{3\pi R^2 \hat{R}} \left(\frac{R_e}{\hat{R}}\right)^{-2/3} \frac{R(R - R^*)}{R - R^*} \frac{A_2 R + A_3}{A_2 R_e + A_3} \exp(B_1 + B_2) \tag{5}$$

where

$$B_1 = \frac{A_2}{\tau A_1}\left[\frac{{R_e}^2 - R^2}{2} + R^*(R_e - R) - {R^*}^2 \ln\left(\frac{R - R^*}{R_e - R^*}\right)\right] \tag{6}$$

$$B_2 = \frac{A_2}{\tau A_1}\left[R_e - R - R^* \ln\left(\frac{R - R^*}{R_e - R^*}\right)\right] \tag{7}$$

$$\tau = \frac{3{R_e}^2 (A^2 R_e + A_3)^2}{A_1(11 A_2 {R_e}^2 - 14 A_2 R_e R^* + 8 A_3 R_e - 11 A_3 R^*)} \tag{8}$$

$$A_1 = \frac{\Delta T}{h_{fg} \rho_w (1 - \cos\theta)^2 (2 + \cos\theta)} \tag{9}$$

$$A_2 = \frac{\theta}{4 k_w \sin\theta} \tag{10}$$

$$A_3 = \frac{1}{2 h_i (1 - \cos\theta)} + \frac{1}{k_{HC} \sin^2\theta)}\left[\frac{k_P \phi}{\delta_{HC} k_P + h k_{HC}} + \frac{k_w (1 - \phi)}{\delta_{HC} k_w + h k_{HC}}\right]^{-1} \tag{11}$$

$\hat{R}$ is the average maximum droplet radius (departure radius), τ is the droplet sweeping period, and R_e is the radius when droplets growing by direct vapor addition begin to merge and grow by droplet coalescence, $R_e = l_c/2$. For large droplets growing mainly due to coalescence, the droplet distribution $N(R)$ was determined from[17]

$$N(R) = \frac{1}{3\pi R^2 \hat{R}} \left(\frac{R_e}{\hat{R}}\right)^{-2/3} \tag{12}$$

The total surface steady state condensation heat flux, q'', was obtained by incorporating the individual droplet heat transfer rate (eq 1) with the droplet size distributions (eqs 5 and 12)

$$q'' = \int_{R^*}^{R_e} q(R) n(R) \mathrm{d}R + \int_{R_e}^{\hat{R}} q(R) N(R) \mathrm{d}R \tag{13}$$

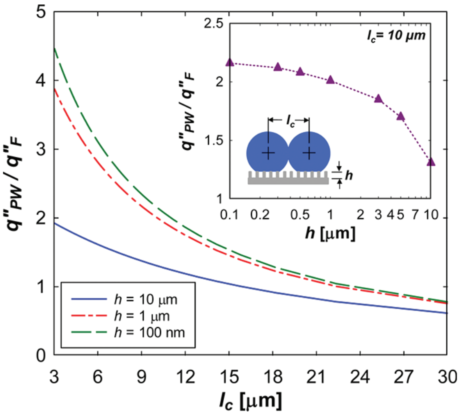

Figure 6. Theoretical heat flux ratio (q''_{PW}/q''_F) of a surface favoring PW droplet formation (q''_{PW}) compared to a flat hydrophobic surface (q''_F) as a function of coalescence length (l_c) and pillar height (h); $l_c = 2R_e = 2\hat{R}$ for the PW surface, and $l_c = 2R_e = 28 \pm 7$ μm for the F surface. As expected, the heat flux ratio increases as h decreases due to the diminishing P-C-G thermal resistance. In addition, reducing l_c acts to increase the heat transfer ratio due to earlier droplet removal from the surface and higher population of small droplets.[23] Inset: Heat flux ratio (q''_{PW}/q''_F) as a function of h for the experimentally measured coalescence length, $l_c = 10 \pm 2$ μm.

For droplets growing on the flat surface (F), $\hat{R}$ was assumed to be 2 mm,[10] and $l_c = 2R_e = 28 \pm 7$ μm. Droplet growth on the structured surface above the coalescence length for both PW and S morphologies was neglected because most droplets coalesced and ejected from the surface.[15] In addition, the sweeping time τ was assumed to be infinite on the nanostructured surface due to the coalescence-induced ejection departure mechanism, and $l_c = 2R_e = 2\hat{R} = 10 \pm 2$ μm. Figure 5 shows the total surface heat flux, q'', as a function of the difference between the wall and saturation temperature, ΔT, for these surfaces with the three identified wetting morphologies (PW, S, and F). As expected, the structured surface with the PW wetting morphology showed a 56% heat flux *enhancement* when compared to that of the flat surface. Meanwhile, a 71% heat flux *degradation* was shown for the surface with the S wetting morphology which indicated the increased thermal resistance and the slower growth rate prior to coalescence outweighed the benefits of droplet ejection. Figure 5 indicates that meeting the criteria of Cassie stability is not the only requirement for heat and mass transfer enhancement *via* nanostructuring.

This comparison (Figure 5) assumed that only PW or S droplet morphologies existed exclusively on the structured surfaces. In actuality, approximately the same number of PW and S wetting morphologies were observed on the nanostructured surface in this work, resulting in a total surface heat flux degradation of 12% when compared to the flat hydrophobic surface.

It is important to note that the difference in observed coalescence lengths between the flat and structured surfaces contributed to the heat and mass transfer performance. To control for this parameter, we investigated the hypothetical case where the coalescence length for all three droplet morphologies is equivalent, $l_{c,PW} = l_{c,S} = l_{c,F} = 10 \pm 2\ \mu$m. For the hypothetical case, the PW and S wetting morphologies showed an 11% enhancement and an 80% degradation compared to the flat surface, respectively. As expected, the PW enhancement decreased and S degradation increased due to the higher heat and mass transfer of the F morphology associated with the increased population of droplets with radii below the coalescence length.[1,16,17]

To gain a broader understanding of the P-C-G thermal resistance, the developed model was used to investigate the effect of pillar height (h) and coalescence length (l_c) on the PW to F heat flux ratio (q''_{PW}/q''_F) (Figure 6). This comparison assumed $l_c = 2R_e = 2\hat{R}$ for the PW surface, $l_c = 2R_e = 28 \pm 7\ \mu$m for the F surface, and that scaling down the pillar height does not affect the PW surface wetting state or contact angle behavior. As expected, the results show that the heat flux ratio increases as h decreases due to the smaller P-C-G thermal resistance. In addition, a reduction in l_c acts to increase the heat transfer ratio due to earlier droplet removal from the surface and a higher population of smaller droplets.[15] The results of these analyses further emphasize the conclusion that structured surface droplet wetting morphology needs to be carefully controlled to realize enhanced condensation heat and mass transfer. Furthermore, the analysis suggests the importance of minimizing the thermal resistance of the PW morphology (*i.e.*, by reducing pillar height), while ensuring Cassie stability to achieve dropwise condensation heat and mass transfer enhancement *via* surface structuring.

CONCLUSIONS

In summary, we demonstrated the importance of droplet wetting morphology on condensation growth rates for Cassie stable surfaces *via* an *in situ* ESEM study of S and PW droplet morphologies on superhydrophobic nanostructured surfaces. While both droplet morphologies demonstrated coalescence-induced droplet ejection at identical length scales, the initial growth rate of the PW morphology was 6× higher than that of the S morphology due to the increased contact with the substrate. Additionally, transitioning S to PW droplets showed a rapid 2.8× increase in growth rate due to the change in wetting morphology and surface subcooling. The experimental results were corroborated with a thermal resistance-based droplet growth model and showed that PW droplets had a 4−6× higher heat transfer rate than S droplets for the observed coalescence lengths. On the basis of these results, which showed the importance of droplet wetting morphology on individual droplet heat and mass transfer, we investigated the overall performance of the structured surface compared to a flat hydrophobic surface. Using droplet distribution theory combined with the droplet growth model, we showed that these nanostructured surfaces with PW morphologies had 56% total surface heat flux enhancement, while S morphologies had 71% heat flux degradation when compared to a flat hydrophobic surface. These results shed light on the previously unidentified importance of droplet wetting morphology for dropwise condensation heat and mass transfer on superhydrophobic nanostructured surfaces as well as the importance of designing Cassie stable nanostructured surfaces with tailored droplet morphologies to achieve enhanced heat and mass transfer during dropwise condensation.

METHODS

Fabrication Procedure of Silicon Nanopillars. Silicon nanopillar surfaces (Figure 1A) with diameters of d = 300 nm, heights of h = 6.1 μm, and center-to-center spacings of l = 2 μm (solid fraction $\varphi = \pi d^2/4l^2 = 0.0177$ and roughness factor $r = 1 + \pi dh'/l^2 = 3.26$) were fabricated using e-beam lithography and deep reactive ion etching. Chemical vapor deposition (CVD) of (tridecafluoro-1,1,2,2-tetrahydrooctyl)-1-trichlorosilane was used to functionalize and create Cassie stable superhydrophobic surfaces (see section S2 of Supporting Information). The samples were first cleaned in a plasma cleaner (Harrick Plasma) for 20 min, then immediately placed in a vacuum chamber containing an open container of silane at room temperature and held at 17.5 kPa for 30 min. Upon removal from the chamber, the samples were rinsed in ethanol and DI water and then dried with N_2. Goniometric measurements on a smooth silanated silicon surface showed an advancing and receding contact angle of $\theta_a = 119.2 \pm 1.3°$ and $\theta_r = 86.1 \pm 1.3°$, respectively.

ESEM Imaging Procedure. Condensation nucleation and growth were studied on these fabricated surfaces using an environmental scanning electron microscope (EVO 55 ESEM, Zeiss). Backscatter detection mode was used with a high gain. The water vapor pressure in the ESEM chamber was 1200 ± 12 Pa. The sample temperature was set to 9 ± 1.5 °C using a cold stage, resulting in nucleation of water droplets on the sample surface from the saturated water vapor. Typical image capture was obtained with a beam potential of 20 kV and variable probe current depending on the stage inclination angle. To limit droplet heating effects,[26] probe currents were maintained below 1.9 nA and the view area was kept above 400 μm × 300 μm. A 500 μm lower aperture was used in series with a 1000 μm variable pressure upper aperture to obtain greater detail. The sample temperature was initially set to 10 ± 1.5 °C and was allowed to equilibrate for 5 min. The surface temperature was subsequently decreased to 9 ± 1.5 °C, resulting in nucleation of water droplets on the sample surface. Images and recordings were obtained at an inclination angle of 70−80° from the horizontal to observe growth dynamics and wetting morphologies close to the droplet base. Recordings were obtained at 2.5 s time increments corresponding to 0.4 fps. Copper tape was used for mounting the sample to the cold stage to ensure good thermal contact.

Conflict of Interest: The authors declare no competing financial interest.

Acknowledgment. The authors acknowledge Rong Yang and Professor Karen Gleason from the MIT Chemical Engineering Department for help in performing iCVD on the smooth pillar samples. The authors acknowledge the support from the MIT S3TEC Center, an Energy Frontier Research Center funded by the Department of Energy, Office of Science, Office of Basic Energy Sciences. N.M. acknowledges funding support from the Natural Sciences and Engineering Research Council of Canada. R.E. acknowledges support from the Irish Research Council for Science, Engineering, and Technology, cofunded by Marie Curie Actions under FP7. This work was performed in part at the Center for Nanoscale Systems (CNS), a member of the National Nanotechnology Infrastructure Network (NNIN), which is supported by the National Science Foundation under NSF award number ECS-0335765. CNS is part of Harvard University.

Supporting Information Available: Four videos showing all condensation processes, as well as further information on data collection methodology, the energetically favored wetting state, dynamic droplet contact angles, suspended droplet pinning due to pillar scallops, droplet coalescence and removal, droplet growth modeling, transitioning droplet surface subcooling, and flat surface droplet growth. This material is available free of charge *via* the Internet at http://pubs.acs.org.

REFERENCES AND NOTES

1. Glicksman, L. R.; Hunt, A. W. Numerical Simulation of Dropwise Condensation. *Int. J. Heat Mass Transfer* **1972**, *15*, 2251–2269.
2. Love, J. C.; Estroff, L. A.; Kriebel, J. K.; Nuzzo, R. G.; Whitesides, G. M. Self-Assembled Monolayers of Thiolates on Metals as a Form of Nanotechnology. *Chem. Rev.* **2005**, *105*, 1103–1169.
3. Andrews, H. G.; Eccles, E. A.; Schofield, W. C. E.; Badyal, J. P. S. Three-Dimensional Hierarchical Structures for Fog Harvesting. *Langmuir* **2011**, *27*, 3798–3802.
4. Leach, R. N.; Stevens, F.; Langford, S. C.; Dickinson, J. T. Dropwise Condensation: Experiments and Simulations of Nucleation and Growth of Water Drops in a Cooling System. *Langmuir* **2006**, *22*, 8864–8872.
5. Rykaczewski, K.; Scott, J. H. J.; Rajauria, S.; Chinn, J.; Chinn, A. M.; Jones, W. Three Dimensional Aspects of Droplet Coalescence during Dropwise Condensation on Superhydrophobic Surfaces. *Soft Matter* **2011**, *7*, 8749–8752.
6. Milani, D.; Abbas, A.; Vassallo, A.; Chiesa, M.; Al Bakri, D. Evaluation of Using Thermoelectric Coolers in a Dehumidification System To Generate Freshwater from Ambient Air. *Chem. Eng. Sci.* **2011**, *66*, 2491–2501.
7. Chen, X.; Wu, J.; Ma, R.; Hua, M.; Koratkar, N.; Yao, S.; Wang, Z. Nanograssed Micropyramidal Architectures for Continuous Dropwise Condensation. *Adv. Funct. Mater.* **2011**, *21*, 4617–4623.
8. Schmidt, E.; Schurig, W.; Sellschopp, W. Versuche über die Kondensation von Wasserdampf in Film- und Tropfenform. *Forsch. Ingenieurwes.* **1930**, *1*, 53–63.
9. Dimitrakopoulos, P.; Higdon, J. J. L. On the Gravitational Displacement of Three-Dimensional Fluid Droplets from Inclined Solid Surfaces. *J. Fluid Mech.* **1999**, *395*, 181–209.
10. Kim, S.; Kim, K. J. Dropwise Condensation Modeling Suitable for Superhydrophobic Surfaces. *J. Heat Transfer* **2011**, *133*, 081502-1–081502-7.
11. Kim, H. Y.; Lee, H. J.; Kang, B. H. Sliding of Liquid Drops down an Inclined Solid Surface. *J. Colloid Interface Sci.* **2002**, *247*, 372–380.
12. Narhe, R. D.; Khandkar, M. D.; Shelke, P. B.; Limaye, A. V.; Beysens, D. A. Condensation-Induced Jumping Water Drops. *Phys. Rev. E* **2009**, *80*, 031604-1–031604-5.
13. Boreyko, J. B.; Chen, C. H. Self-Propelled Dropwise Condensate on Superhydrophobic Surfaces. *Phys. Rev. Lett.* **2009**, *103*, 184501-1–184501-4.
14. Lafuma, A.; Quere, D. Superhydrophobic States. *Nat. Mater.* **2003**, *2*, 457–460.
15. Dietz, C.; Rykaczewski, K.; Fedorov, A. G.; Joshi, Y. Visualization of Droplet Departure on a Superhydrophobic Surface and Implications to Heat Transfer Enhancement during Dropwise Condensation. *Appl. Phys. Lett.* **2010**, *97*, 033104-1–033104-3.
16. Graham, C.; Griffith, P. Drop Size Distributions and Heat Transfer in Dropwise Condensation. *Int. J. Heat Mass Transfer* **1973**, *16*, 337–346.
17. Rose, J. W. On the Mechanism of Dropwise Condensation. *Int. J. Heat Mass Transfer* **1967**, *10*, 755–762.
18. Chen, C. H.; Cai, Q. J.; Tsai, C. L.; Chen, C. L.; Xiong, G. Y.; Yu, Y.; Ren, Z. F. Dropwise Condensation on Superhydrophobic Surfaces with Two-Tier Roughness. *Appl. Phys. Lett.* **2007**, *90*, 173108-1–173108-3.
19. Dietz, C.; Rykaczewski, K.; Fedorov, A.; Joshi, Y. ESEM Imaging of Condensation on a Nanostructured Superhydrophobic Surface. *J. Heat Transfer* **2010**, *132*, 080904-1.
20. Varanasi, K. K.; Hsu, M.; Bhate, N.; Yang, W. S.; Deng, T. Spatial Control in the Heterogeneous Nucleation of Water. *Appl. Phys. Lett.* **2009**, *95*, 094101-1–094101-3.
21. Miljkovic, N.; Enright, R.; Maroo, S. C.; Cho, H. J.; Wang, E. N. Liquid Evaporation on Superhydrophobic and Superhydrophilic Nanostructured Surfaces. *J. Heat Transfer* **2011**, *133*, 080903-1.
22. Lau, K. K. S.; Bico, J.; Teo, K. B. K.; Chhowalla, M.; Amaratunga, G. A. J.; Milne, W. I.; McKinley, G. H.; Gleason, K. K. Superhydrophobic Carbon Nanotube Forests. *Nano Lett.* **2003**, *3*, 1701–1705.
23. Cassie, A. B. D.; Baxter, S. Wettability of Porous Surfaces. *Trans. Faraday Soc.* **1944**, *40*, 546–551.
24. Wenzel, R. N. Resistance of Solid Surfaces to Wetting by Water. *Ind. Eng. Chem.* **1936**, *28*, 988–994.
25. Rykaczewski, K.; Scott, J. H. J. Methodology for Imaging Nano-to-Microscale Water Condensation Dynamics on Complex Nanostructures. *ACS Nano* **2011**, *5*, 5962–5968.
26. Rykaczewski, K.; Scott, J. H. J.; Fedorov, A. G. Electron Beam Heating Effects during Environmental Scanning Electron Microscopy Imaging of Water Condensation on Superhydrophobic Surfaces. *Appl. Phys. Lett.* **2011**, *98*, 093106-1–093106-3.
27. Cao, P. G.; Xu, K.; Varghese, J. O.; Heath, J. R. The Microscopic Structure of Adsorbed Water on Hydrophobic Surfaces under Ambient Conditions. *Nano Lett.* **2011**, *11*, 5581–5586.
28. Anand, S.; Son, S. Y. Sub-Micrometer Dropwise Condensation Under Superheated and Rarefied Vapor Condition. *Langmuir* **2010**, *26*, 17100–17110.
29. Varanasi, K. K.; Deng, T. Controlling Nucleation and Growth of Water Using Hybrid Hydrophobic-Hydrophilic Surfaces. 12th IEEE Intersociety Conference on Thermal and Thermomechanical Phenomena in Electronic Systems, Las Vegas, NV, **2010**; pp 1−5.
30. Rykaczewski, K.; Chinn, J.; Walker, M. L.; Scott, J. H. J.; Chinn, A.; Jones, W. Dynamics of Nanoparticle Self-Assembly into Superhydrophobic Liquid Marbles during Water Condensation. *ACS Nano* **2011**, *5*, 9746–9754.
31. Moulinet, S.; Bartolo, D. Life and Death of a Fakir Droplet: Impalement Transitions on Superhydrophobic Surfaces. *Eur. Phys. J. E* **2007**, *24*, 251–260.
32. Tanaka, H.; Tsuruta, T. A Microscopic Study of Dropwise Condensation. *Int. J. Heat Mass Transfer* **1984**, *27*, 327–335.
33. Tam, D.; von Arnim, V.; McKinley, G. H.; Hosoi, A. E. Marangoni Convection in Droplets on Superhydrophobic Surfaces. *J. Fluid Mech.* **2009**, *624*, 101–123.
34. Umur, A.; Griffith, P. Mechanism of Dropwise Condensation. *J. Heat Transfer* **1965**, *87*, 275–282.
35. Mikic, B. B. On Mechanism of Dropwise Condensation. *Int. J. Heat Mass Transfer* **1969**, *12*, 1311–1323.

36. Narhe, R. D.; Beysens, D. A. Nucleation and Growth on a Superhydrophobic Grooved Surface. *Phys. Rev. Lett.* **2004**, *93*, 076103-1–076103-4.
37. Narhe, R. D.; Beysens, D. A. Water Condensation on a Super-Hydrophobic Spike Surface. *Europhys. Lett.* **2006**, *75*, 98–104.
38. Narhe, R. D.; Gonzalez-Vinas, W.; Beysens, D. A. Water Condensation on Zinc Surfaces Treated by Chemical Bath Deposition. *Appl. Surf. Sci.* **2010**, *256*, 4930–4933.
39. Beysens, D. Dew Nucleation and Growth. *CR Phys.* **2006**, *7*, 1082–1100.
40. Beysens, D.; Steyer, A.; Guenoun, P.; Fritter, D.; Knobler, C. M. How Does Dew Form? *Phase Transitions* **1991**, *31*, 219–246.
41. Fritter, D.; Knobler, C. M.; Beysens, D. A. Experiments and Simulation of the Growth of Droplets on a Surface (Breath Figures). *Phys. Rev. A* **1991**, *43*, 2858–2869.
42. Steyer, A.; Guenoun, P.; Beysens, D.; Knobler, C. M. Growth of Droplets on a Substrate by Diffusion and Coalescence. *Phys. Rev. A* **1991**, *44*, 8271–8277.
43. Hirth, J. P.; Pound, G. M. *Condensation and Evaporation*; Macmillan: New York, 1963; p xvi, 191 p. (p. 191 advertisement).
44. Kaschiev, D. *Nucleation: Basic Theory with Applications*; Butterworth Heinemann: Oxford, 2000.
45. Sigsbee, R. A. Adatom Capture and Growth Rates of Nuclei. *J. Appl. Phys.* **1971**, *42*, 3904–3915.